A New Growing Method for Simplex-Based Endmember Extraction Algorithm

Chein-I Chang, *Senior Member, IEEE*, Chao-Cheng Wu, *Student Member, IEEE*,
Wei-min Liu, *Student Member, IEEE*, and Yen-Chieh Ouyang, *Member, IEEE*

***Abstract*—A new growing method for simplex-based endmember extraction algorithms (EEAs), called simplex growing algorithm (SGA), is presented in this paper. It is a sequential algorithm to find a simplex with the maximum volume every time a new vertex is added. In order to terminate this algorithm a recently developed concept, virtual dimensionality (VD), is implemented as a stopping rule to determine the number of vertices required for the algorithm to generate. The SGA improves one commonly used EEA, the N-finder algorithm (N-FINDR) developed by Winter, by including a process of growing simplexes one vertex at a time until it reaches a desired number of vertices estimated by the VD, which results in a tremendous reduction of computational complexity. Additionally, it also judiciously selects an appropriate initial vector to avoid a dilemma caused by the use of random vectors as its initial condition in the N-FINDR where the N-FINDR generally produces different sets of final endmembers if different sets of randomly generated initial endmembers are used. In order to demonstrate the performance of the proposed SGA, the N-FINDR and two other EEAs, pixel purity index, and vertex component analysis are used for comparison.**

***Index Terms*—Endmember extraction, N-finder algorithm (N-FINDR), pixel purity index (PPI), sequential endmember extraction algorithm (SQEEA), simplex growing algorithm (SGA), simultaneous endmember extraction algorithm (SMEEA), vertex component analysis (VCA), virtual dimensionality (VD).**

I. INTRODUCTION

ENDMEMBER extraction has become increasingly important in hyperspectral image analysis due to significantly improved high spatial and spectral resolution provided by hyperspectral imaging sensors. According to the definition given in [1], an endmember is an idealized, pure signature for a class. For multispectral imagery, an endmember may be difficult to find since most image pixels are heavily mixed because of low spatial and spectral resolution. As a result, the importance of endmember extraction has been overlooked, and its issue has not been a major subject in multispectral image analysis. By contrast, with advances of hyperspectral imaging sensors many subtle material substances that cannot be resolved by multispectral imagery can now be uncovered by hyperspectral imagery. These substances are generally not known *a priori* and can be only diagnosed by high spectral resolution. Endmembers are considered to one type of such substances where their existence in image data cannot be detected visually. Most importantly, once endmembers are present, they may generally appear as anomalies since their population is relatively small. Because of such characteristics, finding endmembers is very challenging. Many algorithms have been developed for this purpose, such as the pixel purity index (PPI) [2], N-finder algorithm (N-FINDR) [3], iterative error analysis (IEA) [4], automated morphological endmember extraction (AMEE) algorithm [5], minimum volume transform (MVT) [6], convex geometry [7], convex cone analysis (CCA) [8], vertex component analysis (VCA) [9], which can be categorized into two classes, simultaneous endmember extraction algorithms (SMEEAs) including PPI, N-FINDR, MVT, CCA, convex geometry, and sequential endmember extraction algorithms (SQEEAs) including IEA, AMEE, and VCA. Technically speaking, an optimal endmember extraction algorithm (EEA) must be an SMEEA. This is because all the endmembers should be selected all together at one time rather than one after another sequentially. However, finding simultaneously endmembers generally requires tremendous computational complexity due to exhaustive search. On the other hand, despite the fact that an SQEEA may not be as optimal as an SMEEA can be, a well-designed SQEEA may be able to perform as well as an SMEEA can. The most advantage benefited from an SQEEA is the significant reduction of computation complexity.

A key idea to design an EEA is to use convexity of the data structure. One such approach is simplex-based methods, which find an appropriate set of vertices that represents desired endmembers in some optimal sense. Among these algorithms is the widely used N-FINDR developed by Winter [3], which finds a simplex of the maximum volume with a given number of vertices p. It is based on an assumption that for a given $(p-1)$-dimensional simplex, the simplex that yields the largest volume will be the one whose p vertices are most likely specified by purest pixels. The vertices of an N-FINDR-found simplex are the desired set of endmembers. Unfortunately, there are several disadvantages of implementing the N-FINDR. One is that there is no provided criterion to determine how many endmembers for the N-FINDR to generate. Another is

---

Manuscript received October 1, 2005; revised July 12, 2006.

C.-I Chang is with the Remote Sensing Signal and Image Processing Laboratory, Department of Computer Science and Electrical Engineering, University of Maryland, Baltimore County, Baltimore, MD 21250 USA, and also with the Department of Electrical Engineering, National Chung Hsing University, Taichung 402, Taiwan, R.O.C. (e-mail: cchang@umbc.edu).

C.-C. Wu and W. Liu are with the Remote Sensing Signal and Image Processing Laboratory, Department of Computer Science and Electrical Engineering, University of Maryland, Baltimore County, Baltimore, MD 21250 USA (e-mail: chaowu1@umbc.edu; weimin1@umbc.edu).

Y.-C. Ouyang is with Department of Electrical Engineering, National Chung Hsing University, Taichung 402, Taiwan, R.O.C. (e-mail: ycouyang@dragon.nchu.edu.tw).

Digital Object Identifier 10.1109/TGRS.2006.881803

that the N-FINDR uses randomly generated vectors as initial endmembers, which are not an effective way to initialize the algorithm. It generally takes a long time to find a desired set of endmembers. Most importantly, due to the nature in the use of random initial endmembers the N-FINDR generally produces different sets of final endmembers at separate runs. Accordingly, how many runs that the N-FINDR must be performed and which set of final generated endmembers by the N-FINDR should be selected as a desired set of endmembers become issues in endmember extraction despite that many of them may be overlapped. Additionally, it is an SMEEA and requires enormous computation to conduct an exhaustive search to find its final set of endmembers. Inspired by the N-FINDR and its drawbacks this paper presents a simplex growing algorithm (SGA) that can be used to resolve these issues commonly encountered in simplex-based algorithms.

As for the first issue in determination of the number of endmembers required to be generated p, there is no guideline suggested in many EEAs [2]–[8]. This issue has been left open. In the SGA, a newly developed concept, called virtual dimensionality (VD) [10], [11], which has recently shown success in determination of the number of endmembers for endmember extraction [9], [12], [13], is proposed to estimate such p. Most recently, a linear mixture model-based least squares error method was proposed to estimate signal subspace in hyperspectral imagery [14]. This method, referred to as signal subspace estimation (SSE) in this paper, can be also used to estimate p. Once p is determined, the N-FINDR starts with a set of p random initial vertices and repeatedly calculates the volumes of new simplexes with new vertex replacements until it finds a simplex with the largest volume. Since the N-FINDR is an SMEEA, the entire process must be repeated over again when each replacement is taken place. Therefore, if the number p is large, the N-FINDR becomes very slow. Our proposed SGA takes a rather different approach. It finds a desired $(p-1)$-dimensional simplex with the largest volume by gradually growing simplexes vertex by vertex. In other words, instead of making an attempt to directly find a p-vertex simplex with the maximum volume, it first finds a two-vertex simplex with the largest volume from which it begins to grow new simplexes with the largest volumes by increasing vertices from 2 to p. Since it generates desired endmembers one by one through a simplex growing process, the SGA is an SQEEA. With such a simplex growing implementation, the SGA only has to find one endmember at a time until it reaches a desired number of endmembers, which is the VD-estimated p. This is completely different from the N-FINDR, which is an SMEEA and replaces vertices of simplexes with a number of newfound vertices repeatedly. A third issue for the N-FINDR is a consequence resulting from its use of random vectors as initial endmembers. If the N-FINDR is rerun again, it is most likely that a different set of final endmembers is generated due to the use of a different set of random initial vectors. The SGA resolves this issue by judiciously selecting the initial vectors to initialize the algorithm. Accordingly, the final generated set of endmembers is always the same and consistent.

Incidentally, a recent VCA approach developed in [9] is similar to the SGA from two aspects. Both use the VD to estimate the number of endmembers required to be generated. Besides, both also grow simplexes gradually vertex by vertex to find desired endmembers. However, there are also two distinct features between the VCA and the SGA. The VCA repeatedly performs orthogonal subspace projections resulting from a sequence of gradual growing simplexes vertex by vertex to find new vertices. By contrast, the SGA finds maximum volumes for a sequence of gradual growing simplexes vertex by vertex. Furthermore, the SGA develops a specific algorithm to generate initial endmembers so that the final selection of endmembers by the SGA is consistent regardless of how many runs the SGA is implemented. But, like the N-FINDR, the VCA makes use of a zero-mean Gaussian distribution to generate a random vector as its initial projection for each simplex it grows. As a result, the VCA suffers from the same drawback as does the N-FINDR. That is, final sets of endmembers generated by the VCA in different runs are usually not consistent.

In order to demonstrate the performance of the proposed SGA, a comparative analysis among the SGA, PPI, N-FINDR, and VCA is conducted via synthetic image-based computer simulations as well as two real hyperspectral image data where experimental results show that the SGA generally performs significantly better than the N-FINDR in terms of resolving the issues addressed above and also comparable or slightly better than the VCA.

The remainder of this paper is organized as follows. Section II describes an implementation of the N-FINDR developed by Winter [3]. Section III presents a new simplex growing method for endmember extraction, called an SGA. Section IV compares the computational complexity among the PPI, VCA, N-FINDR, and SGA. Sections V and VI conduct a comparative study among the PPI, N-FINDR, VCA, and SGA via synthetic image-based computer simulations and real hyperspectral image experiments for performance analysis and evaluation. Section VII makes concluding remarks.

II. N-FINDER ALGORITHM

The main idea of N-FINDR is to assume that a $(p-1)$-dimensional volume formed by a simplex with p vertices that are specified by the purest pixels is always larger than that formed by another combination of p pixels. N-FINDR was briefly described in [3]. Unfortunately, a detailed step-by-step algorithmic implementation was not provided in [3]. In this section, we summarize the steps to implement N-FINDR according to our understanding and experience as follows. It by no means claims that our interpreted N-FINDR is identical to the one developed by Winter [3]. Nevertheless, the idea used in both algorithms should be the same.

N-FINDR

1) *Preprocessing:*
    a) let p be the number of endmembers required to generate; and
    b) apply a maximum noise fraction (MNF) transformation [or called noise-adjusted principal component (NAPC)] to reduce the data dimensionality from L to $p-1$ where L is the total number of spectral bands.

2) *Initialization:* Let $\{\mathbf{e}_1^{(0)}, \mathbf{e}_2^{(0)}, \ldots, \mathbf{e}_p^{(0)}\}$ be a set of initial vectors randomly generated from the data.
3) At iteration $k \geq 0$, find $V(\mathbf{e}_1^{(k)}, \mathbf{e}_2^{(k)}, \ldots, \mathbf{e}_p^{(k)})$ defined by

$$V\left(\mathbf{e}_1^{(k)}, \ldots, \mathbf{e}_p^{(k)}\right) = \frac{\left|\det \begin{bmatrix} 1 & 1 & \ldots & 1 \\ \mathbf{e}_1^{(k)} & \mathbf{e}_2^{(k)} & \ldots & \mathbf{e}_p^{(k)} \end{bmatrix}\right|}{(p-1)!} \quad (1)$$

which is the volume of the simplex with vertices $\mathbf{e}_1^{(k)}, \mathbf{e}_2^{(k)}, \ldots, \mathbf{e}_p^{(k)}$, denoted by $S(\mathbf{e}_1^{(k)}, \mathbf{e}_2^{(k)}, \ldots, \mathbf{e}_p^{(k)})$.
4) *Stopping rule:* For each sample vector $\mathbf{r}$, we recalculate $V(\mathbf{r}, \mathbf{e}_2^{(k)}, \ldots, \mathbf{e}_p^{(k)})$, $V(\mathbf{e}_1^{(k)}, \mathbf{r}, \mathbf{e}_3^{(k)}, \ldots, \mathbf{e}_p^{(k)})$, $\ldots, V(\mathbf{e}_1^{(k)}, \ldots, \mathbf{e}_{p-1}^{(k)}, \mathbf{r})$, the volumes of p simplexes, $S(\mathbf{r}, \mathbf{e}_2^{(k)}, \ldots, \mathbf{e}_p^{(k)})$, $S(\mathbf{e}_1^{(k)}, \mathbf{r}, \mathbf{e}_3^{(k)}, \ldots, \mathbf{e}_p^{(k)}), \ldots$, $S(\mathbf{e}_1^{(k)}, \mathbf{e}_2^{(k)}, \ldots, \mathbf{e}_{p-1}^{(k)}, \mathbf{r})$, each of which is formed by replacing one endmember $\mathbf{e}_j^{(k)}$ with the sample vector $\mathbf{r}$. If none of these p recalculated volumes, $V(\mathbf{r}, \mathbf{e}_2^{(k)}, \ldots, \mathbf{e}_p^{(k)})$, $V(\mathbf{e}_1^{(k)}, \mathbf{r}, \mathbf{e}_3^{(k)}, \ldots, \mathbf{e}_p^{(k)})$, $\ldots, V(\mathbf{e}_1^{(k)}, \ldots, \mathbf{e}_{p-1}^{(k)}, \mathbf{r})$, is greater than $V(\mathbf{e}_1^{(k)}, \mathbf{e}_2^{(k)}, \ldots, \mathbf{e}_p^{(k)})$, no endmember in $\mathbf{e}_1^{(k)}, \mathbf{e}_2^{(k)}, \ldots, \mathbf{e}_p^{(k)}$ will be replaced. The algorithm is terminated. Otherwise, continue.
5) *Replacement rule:* The endmember pixel which is absent in the largest volume among the p simplexes, $S(\mathbf{r}, \mathbf{e}_2^{(k)}, \ldots, \mathbf{e}_p^{(k)})$, $S(\mathbf{e}_1^{(k)}, \mathbf{r}, \mathbf{e}_3^{(k)}, \ldots, \mathbf{e}_p^{(k)})$, $\ldots$, $S(\mathbf{e}_1^{(k)}, \mathbf{e}_2^{(k)}, \ldots, \mathbf{e}_{p-1}^{(k)}, \mathbf{r})$, will be replaced by the sample vector $\mathbf{r}$. Assume that such an endmember is denoted by $\mathbf{e}_j^{(k+1)}$. A new set of endmembers is then produced by letting $\mathbf{e}_j^{(k+1)} = \mathbf{r}$ and $\mathbf{e}_i^{(k+1)} = \mathbf{e}_i^{(k)}$ for $i \neq j$. Let $k \leftarrow k+1$ and go to step 3).

III. SIMPLEX GROWING ALGORITHM

Since an endmember is an idealized pure signature, it is not necessarily an image pixel. However, in real-image experiments, an endmember is generally extracted directly from the data. Therefore, when it occurs as a pixel, it is referred to as endmember pixel in this paper.

In this section, we present a new algorithm, called SGA, for endmember extraction to find a set of desired endmembers by growing a sequence of simplexes. It starts off with two vertices and begins to grow a simplex by increasing its vertices one at a time. The algorithm is terminated when the number of vertices reaches the number of endmembers p, which can be estimated by the VD using a method developed by Harsanyi, Farrand, and Chang, referred to as HFC method in [10], which does not require noise estimation. In order to select an appropriate pixel as its initial endmember pixel, a selection process for finding the first endmember pixel is developed for this purpose and described as follows.

First Endmember Selection Process

1) Randomly generate a target pixel, denoted by $\mathbf{t}$.
2) Find a pixel $\mathbf{e}_1$ that yields the maximum of absolute determinant of the matrix, $\left|\det \begin{bmatrix} 1 & 1 \\ \mathbf{t} & \mathbf{r} \end{bmatrix}\right|$ over all sample vectors $\mathbf{r}$, i.e.,

$$\mathbf{e}_1 = \arg\left\{\max_{\mathbf{r}} \left[\left|\det \begin{bmatrix} 1 & 1 \\ \mathbf{t} & \mathbf{r} \end{bmatrix}\right|\right]\right\}$$

where principal components analysis (PCA) or MNF is required to reduce the original data dimensionality L to the dimension 2 to find the maximum.

It is worth noting that the generation of the first endmember pixel $\mathbf{e}_1$ is determined by the randomly generated target pixel $\mathbf{t}$. A different target pixel $\mathbf{t}$ may result in a different $\mathbf{e}_1$. Interestingly, the experiments show that the generated $\mathbf{e}_1$ is always a pixel which has either a maximum or a minimum value in the first component of dimensionality reduction (DR) transform. Therefore, the target pixel $\mathbf{t}$ has no effect on the final set of endmembers. Furthermore, according to our extensive experiments, the generated $\mathbf{e}_1$ eventually becomes one of the final generated endmembers. This explains that the final set of endmembers generated by the SGA is always the same and consistent.

Including the above first endmember selection process as a preprocessing for initialization, the SGA can be described in detail as follows.

Simplex Growing Algorithm

1) *Initialization:*
   a) use the VD to estimate the number of endmembers to be generated p; and
   b) use the $\mathbf{e}_1$ found by the first endmember selection process as the desired initial endmember pixel and set $n = 1$.
2) At $n \geq 1$ and for each sample vector $\mathbf{r}$, we calculate $V(\mathbf{e}_1, \ldots, \mathbf{e}_n, \mathbf{r})$ defined by

$$V(\mathbf{e}_1, \ldots, \mathbf{e}_n, \mathbf{r}) = \frac{\left|\det \begin{bmatrix} 1 & 1 & \ldots & 1 & 1 \\ \mathbf{e}_1 & \mathbf{e}_2 & \ldots & \mathbf{e}_n & \mathbf{r} \end{bmatrix}\right|}{n!} \quad (2)$$

which is the volume of the simplex specified by vertices $\mathbf{e}_1, \mathbf{e}_2, \ldots, \mathbf{e}_n, \mathbf{r}$, denoted by $S(\mathbf{e}_1, \mathbf{e}_2, \ldots, \mathbf{e}_n, \mathbf{r})$. Since the matrix $\begin{bmatrix} 1 & 1 & \ldots & 1 & 1 \\ \mathbf{e}_1 & \mathbf{e}_2 & \ldots & \mathbf{e}_n & \mathbf{r} \end{bmatrix}$ in (2) is not necessarily a square matrix, a DR technique such as PCA or MNF is required to reduce the original data dimensionality L to the dimension n.
3) Find $\mathbf{e}_{n+1}$ that yields the maximum of (2), i.e.,

$$\mathbf{e}_{n+1} = \arg\left\{\max_{\mathbf{r}} \left[V(\mathbf{e}_1, \ldots, \mathbf{e}_n, \mathbf{r})\right]\right\}. \quad (3)$$

4) *Stopping rule:* If $n < p$, then $n \leftarrow n+1$ and go step 2). Otherwise, the final set of $\{\mathbf{e}_1, \mathbf{e}_2, \ldots, \mathbf{e}_p\}$ is the desired p endmembers.

TABLE I
COMPUTATIONAL COMPLEXITY AMONG PPI, N-FINDR, VCA, AND SGA

Algorithms	Numbers of flops
PPI	$2psN$
VCA	$2p^2N$
N-FINDR	$p^{\eta+1}N$
SGA	$N\left(\sum_{n=2}^{p} n^{\eta}\right)$

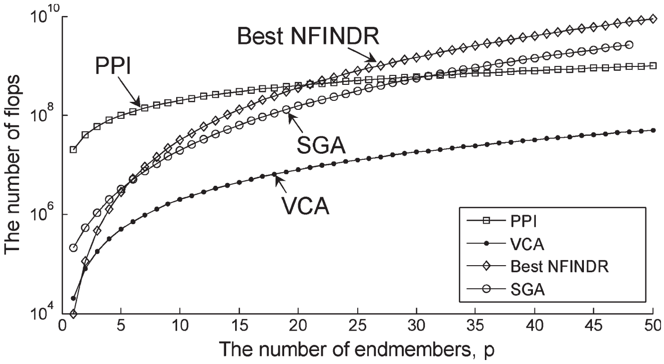

Fig. 1. Plots of numbers of flops versus the number of endmembers, p.

IV. COMPUTATIONAL COMPLEXITY

In this section, a comparative study is conducted on the computational complexity among PPI, VCA, N-FINDR, and SGA. Since the N-FINDR uses randomly generated initial endmembers, it generally results in different numbers of replacements for different runs. Therefore, in this paper, the best N-FINDR was used to compare against the other three algorithms where a best N-FINDR represents a case that no replacement is required for the initial endmembers, in which case the initial endmembers turned out to be the final endmembers. According to the calculation of computational complexity used in [9], approximate numbers of flops (i.e., numbers of floating operations) required for the four EEAs are tabulated in Table I where N is the total number of pixels, p is the number of endmembers, and s is the number of skewers.

Since the computational complexity of performing DR and VD was relatively small and negligible, it was not included in Table I. A best N-FINDR computed the determinant of a $p \times p$ matrix Np times and the computational complexity of each time was p^{η} with $2.3 < \eta < 2.9$. The SGA computes the determinant of a matrix Nn times with n starting from 2 to p. The VCA projected a total of N p-dimensional data vectors onto p orthogonal projections. The PPI projects all data vectors onto a large number of skewers s. Fig. 1 plots the number of flops versus p for each of the four considered EEAs with $N = 10^4$ and $s = 10^3$. As shown in Fig. 1, the number of flops required for the SGA was always less than that required for a best N-FINDR where the VCA had the lowest numbers.

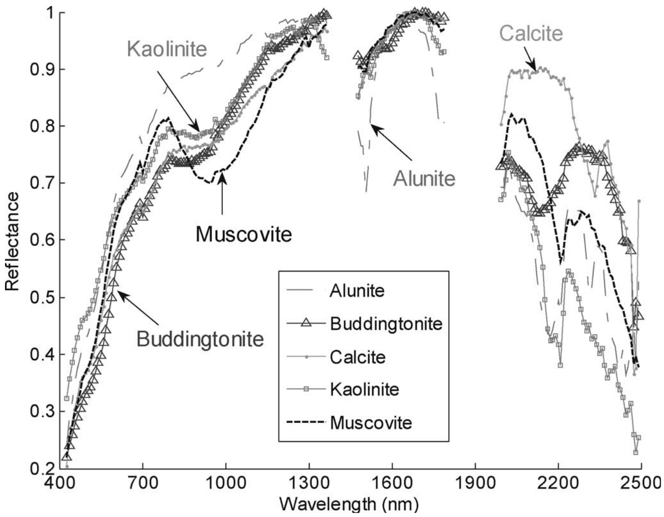

Fig. 2. Five USGS ground-truth mineral spectra.

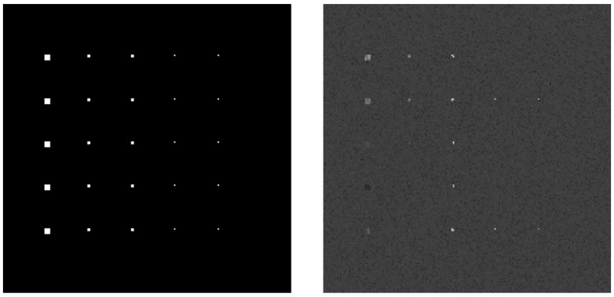

(a) (b)

Fig. 3. (a) Twenty-five simulated panels. (b) A synthetic image having the 25 panels simulated in (a) implanted in the background with an additive Gaussian noise to achieve SNR 20 : 1.

As a concluding remark, a note is worthwhile. In terms of operations implemented in an EEA, the SGA and the N-FINDR as a group, which perform computations of simplex volumes as opposed to the PPI and the VCA as another group, which performs orthogonal projections. Since these two operations are different in nature, it may not be a fair comparison between these two groups. However, Fig. 1 shows that within each group, the SGA and VCA were significantly better than the N-FINDR and PPI, respectively. Nevertheless, it should be noted that computing an orthogonal projection is generally faster than that calculating a simplex volume. Accordingly, the VCA yielded the lowest computational cost if the performance is only measured by computing time. As noted, since our proposed SGA is improved from the N-FINDR, it is important to conduct a comparative study on computational complexity between these two. The computation complexity of the PPI and VCA is included in our paper only for reference.

V. COMPUTER SIMULATIONS

In order to conduct a comprehensive comparative analysis, a synthetic image was custom-designed and simulated based on the reflectance spectra of five U.S. Geological Survey (USGS) ground-truth mineral spectra: Alunite (A), Buddingtonite (B), Calcite (C), Kaolinite (K), and Muscovite (M) shown in Fig. 2. It should be noted that the simulated synthetic image may not be realistic from practical applications. But it does allow us to simulate various scenarios to explore many interesting insights that cannot be observed from real image experiments.

The synthetic image has size of 200 × 200 pixel vectors with 25 panels of various sizes that are arranged in a 5 × 5

TABLE II
SIMULATED 20 MIXED PANEL PIXELS IN THE THIRD COLUMN

row 1	$p_{3,11}^{1} = 0.5A + 0.5B$	$p_{3,12}^{1} = 0.5A + 0.5C$
	$p_{3,21}^{1} = 0.5A + 0.5K$	$p_{3,22}^{1} = 0.5A + 0.5M$
row 2	$p_{3,11}^{2} = 0.5A + 0.5B$	$p_{3,12}^{2} = 0.5B + 0.5C$
	$p_{3,21}^{2} = 0.5B + 0.5K$	$p_{3,22}^{2} = 0.5B + 0.5M$
row 3	$p_{3,11}^{3} = 0.5A + 0.5C$	$p_{3,12}^{3} = 0.5B + 0.5C$
	$p_{3,21}^{3} = 0.5C + 0.5K$	$p_{3,22}^{3} = 0.5C + 0.5M$
row 4	$p_{3,11}^{4} = 0.5A + 0.5K$	$p_{3,12}^{4} = 0.5B + 0.5K$
	$p_{3,21}^{4} = 0.5C + 0.5K$	$p_{3,22}^{4} = 0.5K + 0.5M$
row 5	$p_{3,11}^{5} = 0.5A + 0.5M$	$p_{3,12}^{5} = 0.5B + 0.5M$
	$p_{3,21}^{5} = 0.5C + 0.5M$	$p_{3,22}^{5} = 0.5K + 0.5M$

TABLE III
ABUNDANCE FRACTIONS OF SUBPIXEL PANELS IN THE FOURTH AND FIFTH COLUMNS

row	4th column	5th column
1st	$p_{4,11}^{1} = 0.5A + 0.5BKG$	$p_{5,11}^{1} = 0.25A + 0.75BKG$
2nd	$p_{4,11}^{2} = 0.5B + 0.5BKG$	$p_{5,11}^{2} = 0.25B + 0.75BKG$
3rd	$p_{4,11}^{3} = 0.5C + 0.5BKG$	$p_{5,11}^{3} = 0.25C + 0.75BKG$
4th	$p_{4,11}^{4} = 0.5K + 0.5BKG$	$p_{5,11}^{4} = 0.25K + 0.75BKG$
5th	$p_{4,11}^{5} = 0.5M + 0.5BKG$	$p_{5,11}^{5} = 0.25M + 0.75BKG$

matrix and located at the center of the scene shown in Fig. 3(a). The five mineral spectral signatures, $\{\mathbf{m}_i\}_{i=1}^{5}$ in Fig. 2 were used to simulate these 25 panels where each row of five panels was simulated by the same mineral signature and each column of five panels has the same size. Among 25 panels are five 4×4 pure pixel panels for endmember extraction, $p_{4\times 4}^{i}$ for $i = 1, \ldots, 5$ in the first column, five 2×2 pure pixel panels for training samples, $p_{2\times 2}^{i}$ for $i = 1, \ldots, 5$ in the second column, five 2×2 mixed pixel panels, $\{p_{3,jk}^{i}\}_{j=1,k=1}^{2,2}$ for $i = 1, \ldots, 5$ in the third column for mixed pixel classification, five subpixel panels, $p_{4,1}^{i}$ for $i = 1, \ldots, 5$ in the fourth column for subpixel classification and five subpixel panels, $p_{5,1}^{i}$ for $i = 1, \ldots, 5$ in the fifth column for subpixel classification. The reason that the five panels in the second column were included in the image scene was to use them as training samples for supervised classification. The purpose of introducing the five panels in the third column was designed to conduct a study and analysis on five mineral signatures with different mixing in a pixel. Table II tabulates the mixing details of mineral composition in the 20 panels.

The inclusion of the panels in the fourth and fifth columns is to investigate subpixel effect on endmember extraction and their simulated abundance fractions are tabulated in Table III where the background (BKG) was simulated by mixing 20% of each of five mineral signatures, A, B, C, K, and M, i.e., 20%A + 20%B + 20%C + 20%K + 20%M.

These 25 panels in Fig. 3(a) were implanted in the image background in a way that the background pixels were replaced with the implanted panel pixels. Finally, this synthetic image with the 25 implanted panels was corrupted by a simulated white Gaussian noise to achieve signal-to-noise ratio 20 : 1 defined in [10] and [15] as 50% reflectance divided by the standard deviation of the noise. The resulting noisy synthetic is shown in Fig. 3(b). For the synthetic image scene in Fig. 3(b), there are 100 pure pixels, 20 mixed pixels, and 10 subpixels, all of which were simulated by five distinct pure mineral signatures. The VD estimated for this synthetic image was 6 with $P_{\mathrm{F}} \leq 10^{-1}$ that include five mineral signatures, A, B, C, K, M, and the background signature made up of mixing 20% of each minerals, A, B, C, K, and M.

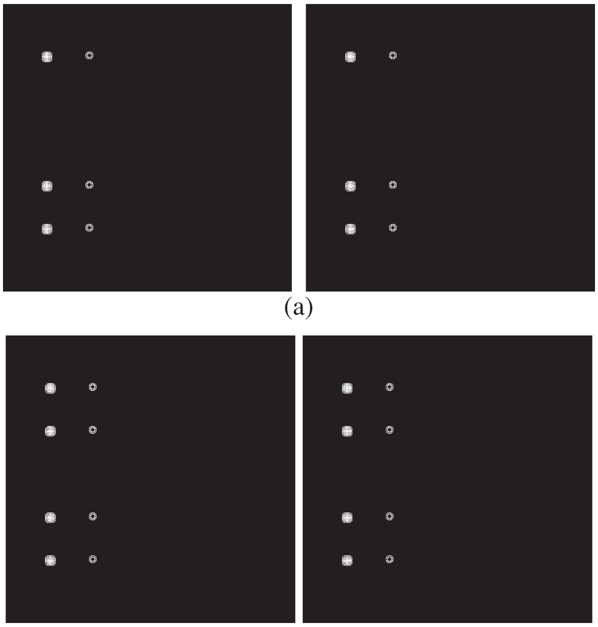
(a)

(b)

Fig. 4. Results of PPI with two different runs using MNF and 50 skewers. (a) VD = 6. (b) SSE = 5.

It should be noted that although the background is equally mixed by five minerals, it is indeed a signature spectrally distinct from the five minerals. This may be due to the fact that the simulated background signature is regarded as a hybrid signature in its own instead of being considered as a mixed signature. As a result, this hybrid signature becomes a new endmember that represents the background class. In this case, the VD counted it as one endmember. Interestingly, a linear mixture model-based least squares error technique recently developed in [14], called SSE can be also used for this purpose where p was estimated to be $p = 5$. In order to see its performance, the results using SSE = 5 were also included in comparison with VD = 6. With the number of endmembers, p estimated by VD = 6 and SSE = 5, two types of EEAs, SMEEA (PPI and N-FINDR), and SQEEA (VCA and SGA) were implemented for comparative analysis.

This experiment is to show a dilemma resulting from the use of randomly generated initial endmembers. That is, final endmembers selected by an EEA are inconsistent. Figs. 4–6 show the final selected endmembers by PPI, N-FINDR, and VCA in two different runs, respectively, where the value of p was estimated by VD and SSE as VD = 6 and SSE = 5. The PPI implemented here was the one described in [2] with number of skewers chosen to be 50.

The N-FINDR found six pixels shown in Fig. 5 where one pixel from each of five 4×4 panels in the first column marked by open circles was extracted in correspondence to

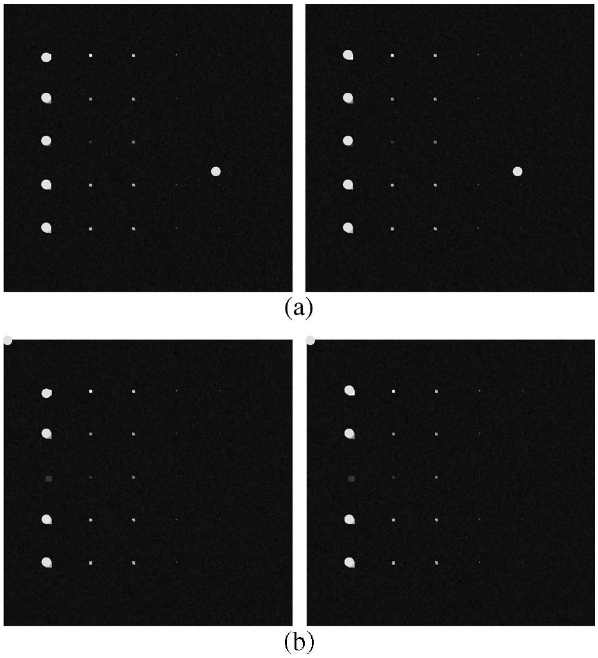

Fig. 5. Results of N-FINDR with two different runs using MNF. (a) VD $= 6$. (b) SSE $= 5$.

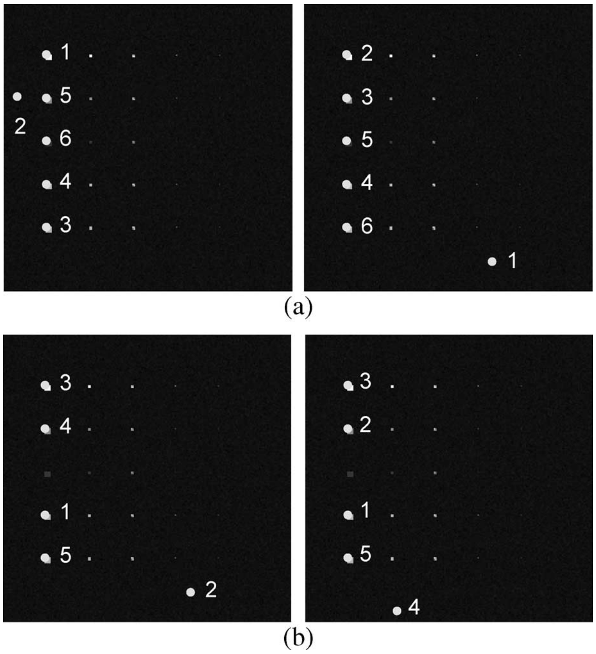

Fig. 6. Results of VCA in two different runs. (a) VD $= 6$. (b) SSE $= 5$.

five pure signatures, A, B, C, K, M, and one background pixel corresponding to a mixed signature was extracted. It should be noted that since the PPI and N-FINDR are SMEEAs, its six endmember pixels were generated simultaneously. Therefore, no numbers were shown in Figs. 4 and 5.

Due to the use of insufficient number of skewers, PPI missed one endmember that represents the signature of the mineral Calcite, but it could be improved to extract all the five endmembers if 500 skewers were used [16]. Additionally, despite that the results shown in Fig. 4 in two different runs looked the same, their PPI counts were actually different.

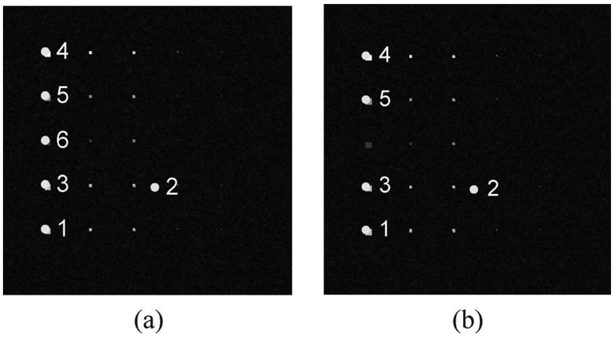

Fig. 7. Results of SGA using MNF. (a) VD $= 6$. (b) SSE $= 5$.

As shown in Figs. 5–7, all three N-FINDR, VCA, and SGA successfully extracted five pixels that were specified by the five pure signatures, A, B, C, K, and M plus one different background pixel that was not an endmember pixel. As also shown in Fig. 6, the background pixels extracted by the VCA in two different runs were different. Additionally, Fig. 6(a) and (b) further shows that the order of the five endmembers corresponding to the five pure signatures, A, B, C, K, M extracted by the VCA in two different runs was also different. This further demonstrated that the results produced by the VCA in different runs were not consistent.

Additionally, Figs. 6 and 7 show the endmember pixels found by the VCA and SGA in two different runs using $p = 5$ and 6, respectively, where the numbers indicated the order of six pixels extracted by the VCA and the SGA in sequence and a background signature was always extracted prior to the last extracted endmember. As a result, when $p = 5$ estimated by the SSE was used, none of the four studied EEAs could extract all five distinct mineral endmembers. They always missed the third panel signature in the first column. On the other hand, if $p = 6$ estimated by the VD was used, all the four EEAs successfully extracted all five minerals. These experiments demonstrated that in order for an EEA to extract all necessary five minerals, the minimum value chosen for p must be at least six estimated by the VD, not five estimated by the SSE.

Since all the four EEAs require DR as a preprocessing prior to endmember extraction. In order to see the impact of different transforms used for DR, three commonly used transforms, PCA, MNF, and independent component analysis (ICA), were implemented to conduct comparative analysis. It should be noted that a problem similar to the use of random initial endmembers in the PPI, N-FINDR, and VCA is also encountered in the ICA implementation, which also uses randomly generated projectors as its initial conditions. In order to mitigate this dilemma, a recent work developed for DR in [17] was implemented as the ICA as DR transform in this paper. Figs. 8–10 show the results of the PPI, N-FINDR, and SGA with VD $= 6$ and SSE $= 5$ where the number of dimensions to be retained after DR was set to be the same as p. It should be noted that no experiments were conducted for the VCA since the algorithm used to run the VCA has its built-in DR transform [9].

By examining the results in Figs. 6 and 8–10, the four EEAs extracted all the five minerals for VD $= 6$ and missed one mineral for SSE $= 5$ regardless of which DR transform was used. This implied that the three DR transforms made very little

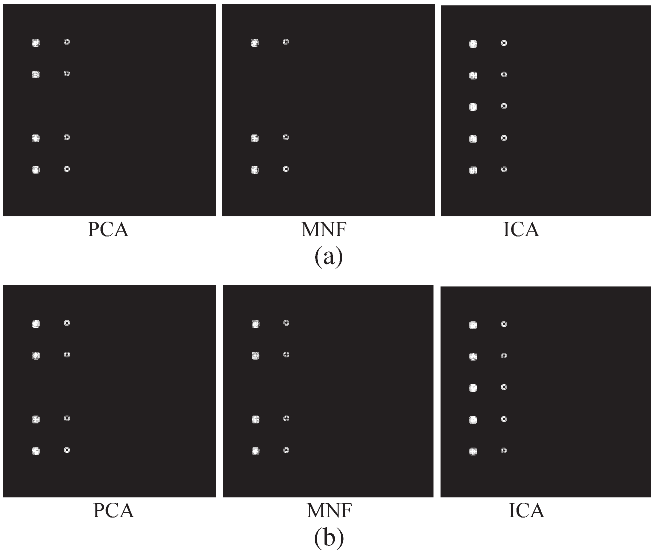

Fig. 8. Endmember pixels extracted by PPI using three different DR transforms. (a) VD = 6. (b) SSE = 5.

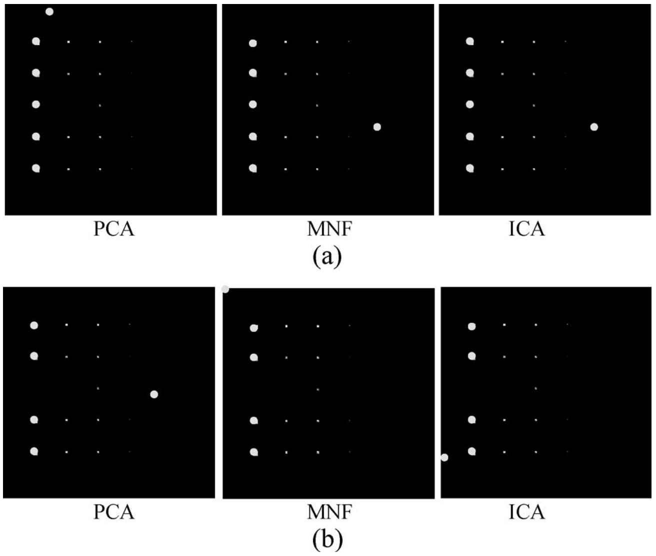

Fig. 9. Endmember pixels extracted by N-FINDR using three different DR transforms. (a) VD = 6. (b) SSE = 5.

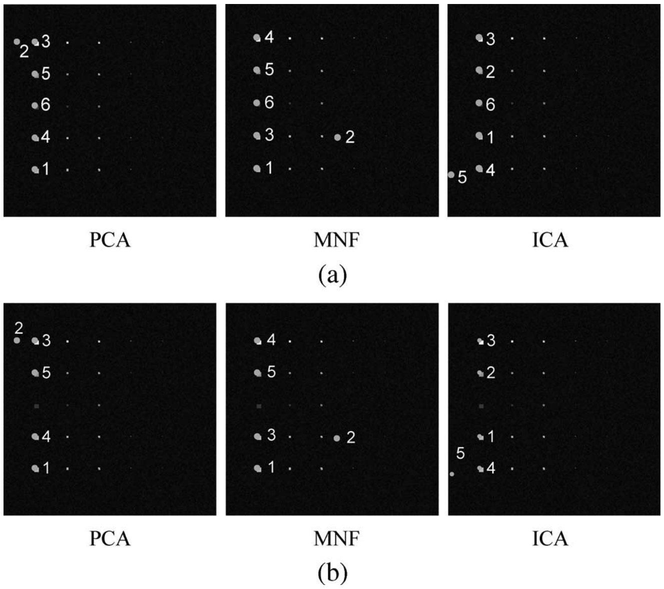

Fig. 10. Endmember pixels extracted by SGA using three different DR transforms. (a) VD = 6. (b) SSE = 5.

TABLE IV
COMPUTING TIME OF PPI, N-FINDR, VCA, AND SGA

Algorithm	PPI (500 skewers)	N-FINDR	VCA	SGA
computing time	7.43 seconds	121.34 seconds	6.9 seconds	27.1 seconds

TABLE V
COMPUTER ENVIRONMENTS USED FOR THE N-FINDR, VCA, AND SGA

CPU	Memory	OS	Kernel version
Intel(R) Xeon (TM) CPU 2.66GHz HT	2 GBytes	Linux	2.4.20

difference in endmember extraction. However, this conclusion will no longer be true as demonstrated in real-image experiments in Section VI. From the above experiments, the only major difference was the value of p for an EEA to generate, in which case VD seemed to provide a better estimate than SSE did.

Table IV tabulates the computing time required for PPI, N-FINDR, VCA, and SGA with $\mathrm{VD} = 6$ using computer environments described in Table V and MATLAB 7.02 service pack 2 where VCA had the best computing time, which was about four times faster than SGA, which was in turn four times faster than N-FINDR where VCA was the most efficient one. However, it is worth noting that in comparison of VCA with SGA their computing time did not truly reflect computational complexity. This is because MATLAB performs "matrix" operations much faster than "for" loops (that is why it is named after Matrix Lab) and the SGA has many more "for" loops than VCA does. Additionally, calculating simplex volume as performed in the SGA generally requires much more computing time than projection carried out in the VCA. It also showed that an SQEEA (i.e., VCA, SGA) is generally much more efficient than an SMEEA (i.e., PPI, N-FINDR).

Three concluding remarks are noteworthy.

1) A prominent difference between SMEEA and SQEEA is that the former searches all the p endmembers simultaneously, while the latter looks for an endmember at a time sequentially. As a result, an SMEEA generally requires an exhaustive search that results in a very high computational complexity. Therefore, to avoid such expensive computing cost, many SMEEAs are actually designed and developed by searching desired endmembers in feasible ranges rather than the entire image. N-FINDR is one which implements step 3) iteratively to replace unlikely endmembers among those already found in a previous iteration with more likely pixels in the current iteration. Therefore, technically speaking, N-FINDR is not an optimal SMEEA. If it is, N-FINDR must replace all the p pixels at a time and find one set of p pixels that yields the maximum simplex volume. In this case, the final p pixels would be desired endmember pixels. Additionally,

the controversy in final inconsistent results resulting from the use of randomly generated initial endmembers can be further avoided because the search is conducted exhaustively in the entire image regardless of which p pixels are picked for processing initially. Unfortunately, such an exhaustive search requires $\binom{N}{p} = N!/(N-p)!p!$ combinations of p pixels. When N becomes large, the searching process also becomes forbidden. This evidence is witnessed by our implementation of CCA [8] for the above synthetic image. Since it is an exhaustive search algorithm, it took tens of hours using the same computer environment implemented by other EEAs to produce the results similar and close to the results presented in this section except different background pixels. Despite that the CCA is of major theoretical interest, it is impractical for applications unless computer environments can be significantly improved to the point that computations are not a major hurdle. Therefore, it is unrealistic to include the CCA experiments in our computational complexity analysis. On the other hand, an SQEEA overcomes this dilemma by producing one endmember at a time sequentially. As a result, its computational complexity can be tremendously reduced. Of course, it is also not an optimal algorithm. Nevertheless, according to our experiments, an SQEEA nearly works as well and effectively as an SMEEA does.

2) As noted in the above experiments, the value of p estimated by the VD and SSE was close, 6 for VD and 5 for SSE. However, in our synthetic image-based simulations, even though SSE differed from the VD by one, the difference between final results in endmember extraction was significant because all the four studied EEAs missed one endmember if $p = 5$. For two SMEEAs, the PPI and N-FINDR missed panels in the third row. For two SQEEAs, the order of the extracted endmembers showed that the VCA and SGA always extracted one background pixel before they extracted the last endmember. In other words, the last extracted endmember always happened to be the sixth pixel. This implies that the background signature must be considered as one of endmembers. This fact was observed in Figs. 5–7 where the background signature was always among the first five extracted signatures, while the fifth mineral signature was always the last and the sixth signature extracted by the N-FINDR, VCA, and SGA. This implies that in order to extract all the five mineral signatures, the least number of endmembers for all the three considered EEAs, N-FINDR, VCA, and SGA to generate must be 6 not 5. In other words, if the number of endmembers is 5, no matter which EEA is implemented, the algorithm always extracts four mineral signatures and one background signature with one missing mineral signature. Therefore, the VD actually provided a more accurate estimate of p than the SSE did. It is also worth noting that according to the definition of endmember given in [1], an endmember is intended to be used to represents a class. In light of this interpretation, $\mathrm{VD} = 6$ is an accurate estimate since there are six classes in the synthetic image in Fig. 3(b), which include five mineral classes plus a background class. This is because the signature that specifies the background class can be considered as a hybrid signature rather than a mixed signature. Furthermore, it can be easily shown that if the OSP classifier in [15] was used to classify the five mineral signatures in Fig. 3(b), using six signatures to form the signature matrix performed better than using only five signatures since the background signature must be used to account for an additional class for background removal so as to achieve better classification.

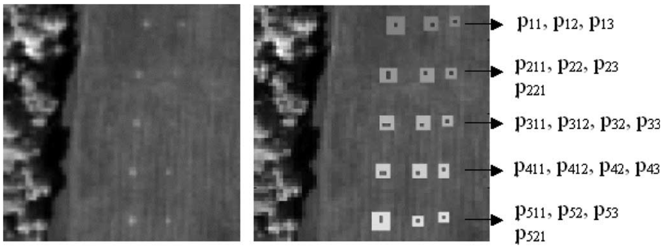

(a) (b)

Fig. 11. (a) HYDICE panel scene that contains 15 panels. (b) Ground truth map of spatial locations of the 15 panels.

3) It is our belief that there are two major issues for the SSE to fail in the above experiments. One is that the SSE is very sensitive to the estimated noise covariance matrix. As a matter of fact, the noise estimation on $\mathrm{SSE} = 5$ is based on multiple regression theory as in [18]. The other issue is the linear mixture model-based least squares error approach used by the SSE. If a hyperspectral image cannot be well represented by a linear mixture model, then it can be expected that the SSE may be very likely to fail. The advantage of the VD over the SSE is that the VD is only determined by the false alarm probability, not by the linear mixture model, nor by noise estimates.

VI. REAL-IMAGE EXPERIMENTS

Two real-image scenes collected by the Hyperspectral Digital Image Collection and Experiment (HYDICE) and Airborne Visible Infrared Imaging Spectrometer (AVIRIS) were used for experiments. The four algorithms, PPI, N-FINDR, VCA, and SGA, were evaluated for performance analysis.

A. *HYDICE Data*

The first image data to be studied consist of an image scene shown in Fig. 11(a), which has a size 64×64 pixel vectors with 15 panels in the scene and the ground truth map in Fig. 11(b) in [10]. It was acquired by 210 spectral bands with a spectral coverage from 0.4 to 2.5 μm. Low signal/high noise bands bands 1–3 and bands 202–210; and water vapor absorption bands: bands 101–112 and bands 137–153 were removed. Therefore, a total of 169 bands were used in experiments. The spatial resolution and spectral resolution of this image scene are 1.56 m and 10 nm, respectively. Within the scene in Fig. 11(a) there is a large grass field background, and a forest on the left edge. Each element in this matrix is a square panel and denoted by p_{ij} with rows indexed by i and columns indexed by

TABLE VI
VD ESTIMATES FOR THE HYDICE SCENE IN Fig. 11 WITH VARIOUS FALSE ALARM PROBABILITIES

	$P_F = 10^{-1}$	$P_F = 10^{-2}$	$P_F = 10^{-3}$	$P_F = 10^{-4}$	$P_F = 10^{-5}$
VD	14	11	9	9	7

$j = 1, 2, 3$. For each row $i = 1, 2, \ldots, 5$, there are three panels painted by the same paint but with three different sizes. The sizes of the panels in the first, second, and third columns are 3×3 m, 2×2 m, and 1×1 m, respectively. Since the size of the panels in the third column is 1×1 m, they cannot be seen visually from Fig. 11(a) due to the fact that its size is less than the 1.56-m pixel resolution. For each column $j = 1, 2, 3$, the five panels have the same size but with five different paints. However, it should be noted that the panels in rows 2 and 3 were made by the same material with two different paints. Similarly, it is also the case for panels in rows 4 and 5. Nevertheless, they were still considered as different panels but our experiments will demonstrate that detecting panels in row 5 (row 4) may also have effect on detection of panels in row 2 (row 3). The 1.56-m spatial resolution of the image scene suggests that most of the 15 panels are one pixel in size except that the panels in the first column with the second, third, fourth, fifth rows, which are two-pixel panels, denoted by $p_{211}, p_{221}, p_{311}, p_{312}, p_{411}, p_{412}, p_{511}, p_{521}$. Fig. 11(b) shows the precise spatial locations of these 15 panels where red pixels (R pixels) are the panel center pixels and the pixels in yellow (Y pixels) are panel pixels mixed with the background.

First of all, the VD was used to estimate number of bands p required for band selection. Table VI calculated the values of VD for the HYDICE image in Fig. 11(a) with various false alarm probabilities.

For our experiments, VD was chosen to be 9. The selection of $p = 9$ is empirical based on the false alarm fixed at probabilities $P_F = 10^{-3}, 10^{-4}$. Once again, the value of p estimated by the SSE was 10.

Experiments similar to those conducted for the synthetic image in Section V were also performed in this section. First of all, we demonstrated inconsistent results of endmembers extracted by the PPI, N-FINDR, and VCA using two different sets of randomly generated initial endmember pixels in two separate runs. Figs. 12–14 show the results of endmember pixels extracted and marked with circles by the three EEAs in two different runs, respectively, where the value of p was estimated by the $\text{VD} = 9$ and $\text{SSE} = 10$ and both PPI and N-FINDR used the MNF for DR. It should be noted that the PPI used 1000 skewers to extract endmember pixels in Fig. 12. For $p = 9$ estimated by the VD, the PPI produced the four panel pixels p_{11}, p_{311}, p_{412}, and p_{521} in one run and another three panel pixels p_{11}, p_{511}, and p_{521} with two panel pixels different which are p_{312} and p_{412}. All the four panel pixels represented four distinct panel signatures, $\mathbf{p}_1$, $\mathbf{p}_3$, $\mathbf{p}_4$, $\mathbf{p}_5$ as endmembers but their PPI counts were different. On the other hand, for $p = 10$ estimated by the SSE, the PPI only extracted three panel pixels, p_{11}, p_{412}, and p_{521} in one run and three panel pixels, p_{11}, p_{312}, and p_{521} in another run. All the extracted panel pixels represented three distinct panel signatures, $\mathbf{p}_1$, $\mathbf{p}_4$, $\mathbf{p}_5$ as endmembers which were one short of four endmembers with $p = 9$. These interesting experiments demonstrated one important observation. That is, a larger $p = 10$ did not guarantee to perform better than a smaller $p = 9$. This is mainly due to two major reasons. One is that unlike an SQEEA which can take advantage of endmembers extracted for a smaller value of p as

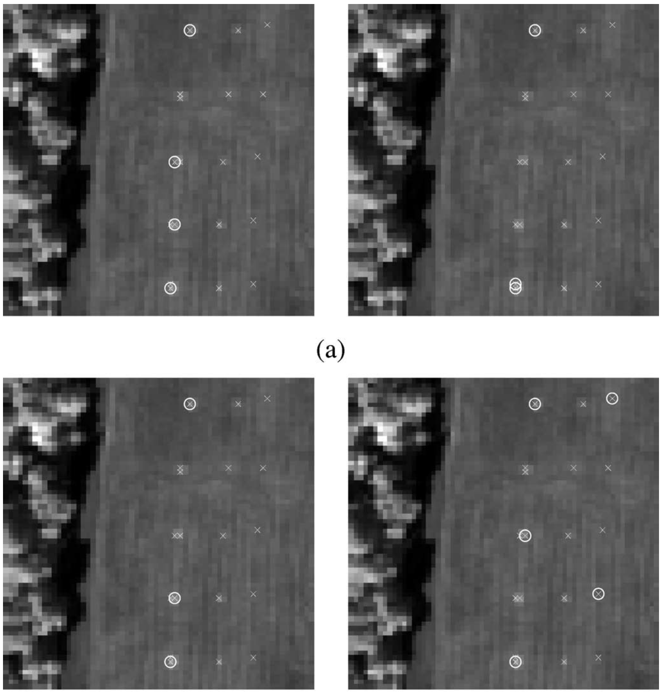
(a)

(b)

Fig. 12. Endmember pixels extracted by PPI with MNF in two different runs. (a) $\text{VD} = 9$. (b) $\text{SSE} = 10$.

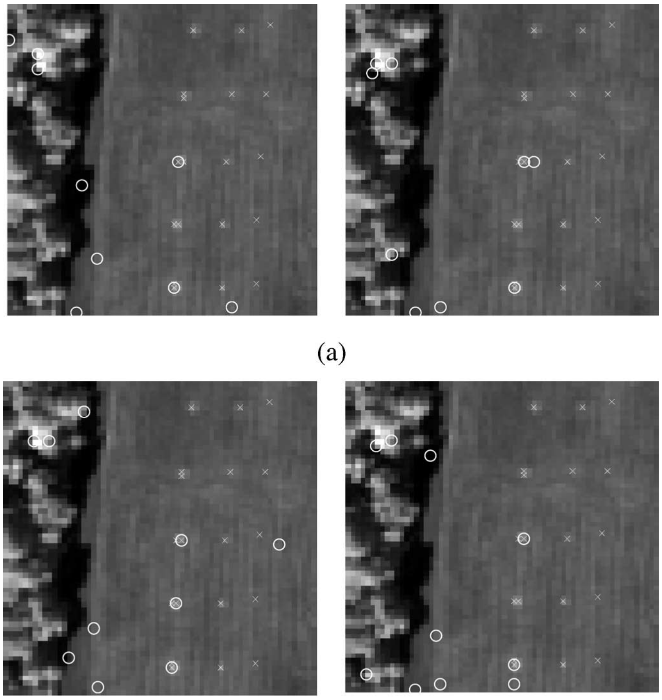
(a)

(b)

Fig. 13. Endmember pixels extracted by N-FINDR with MNF in two different runs. (a) $\text{VD} = 9$. (b) $\text{SSE} = 10$.

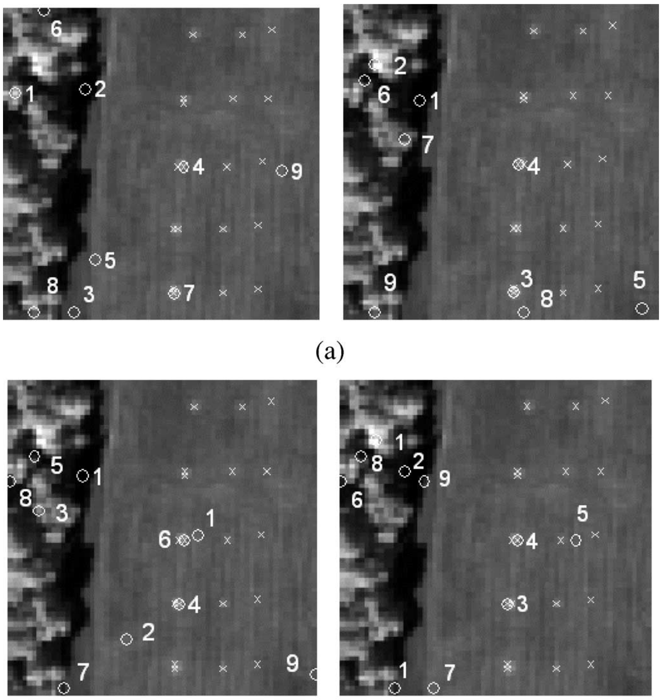

(a)

(b)

Fig. 14. Endmember pixels extracted by VCA in two different runs. (a) VD = 9. (b) SSE = 10.

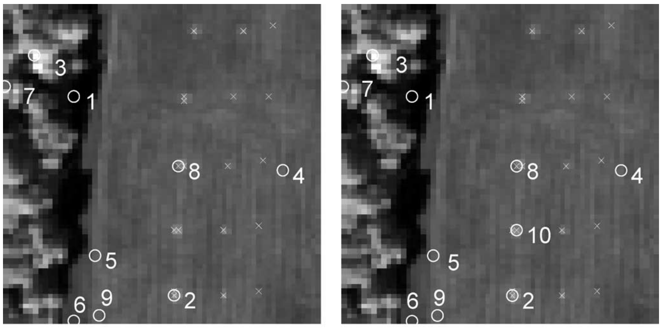

(a) (b)

Fig. 15. Results of SGA using MNF. (a) VD = 9. (b) SSE = 10.

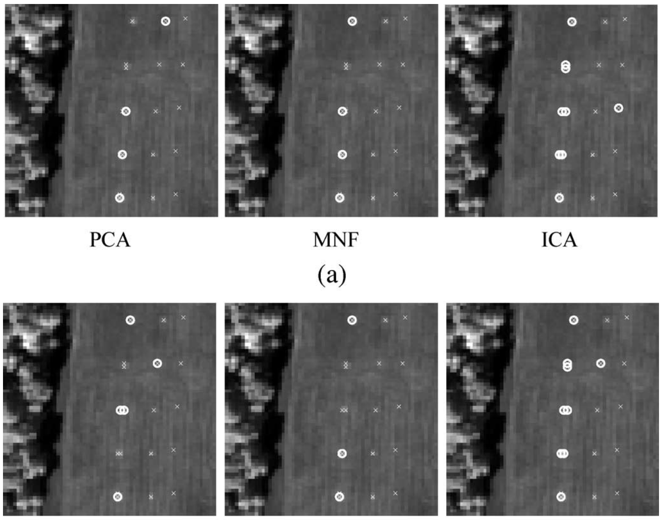

PCA MNF ICA

(a)

PCA MNF ICA

(b)

Fig. 16. Endmember pixels extracted by PPI using three different DR transforms and 1000 skewers. (a) VD = 9. (b) SSE = 10.

part of endmembers generated for a larger value of p, the PPI is an SMEEA and must regenerate all endmembers for different values of p. The other reason is that the PPI produced different PPI counts for endmembers in different runs. In this case, the panel pixel p_{311} that appeared in one run may also disappear in another run due to its low PPI count.

Similarly, N-FINDR also extracted different sets of final endmember pixels in Fig. 13 for both cases, $p = 9$ and 10.

For VD $= 9$, among all extracted pixels are only two were real endmember pixels p_{311} and p_{521} representing two distinct panel signatures $\mathbf{p}_3$ and $\mathbf{p}_5$. However, for SSE $= 10$, three panel pixels p_{311}, p_{412}, and p_{521} were extracted in one run, and two panel pixels p_{311} and p_{521} were extracted in another run.

Fig. 14 also showed that the VCA suffered from the same dilemma encountered in the PPI and N-FINDR where only two panel pixels which might be different were extracted by all the cases. However, it is also interesting to note that VCA extracted different sets of distinct panel signatures in two different runs, $\{\mathbf{p}_3, \mathbf{p}_5\}$ and $\{\mathbf{p}_3, \mathbf{p}_4\}$ for VD $= 9$ and SSE $= 10$, respectively.

Finally, Fig. 15 shows the result produced by our proposed SGA using the MNF as DR for VD $= 9$ and SSE $= 10$ where its performance was at least comparably to the other three EEAs. Since SGA is an SQEEA, the set of endmember pixels extracted by a smaller value of p is always a subset of endmember pixels extracted by a larger value of p. As a result, endmembers extracted in Fig. 15(a) for VD $= 9$ were also endmember pixels in Fig. 15(b) for SSE $= 10$. In this particular case, the tenth extracted endmember pixel occurred to be the panel pixel p_{412}, which represented an additional third panel signature $\mathbf{p}_3$.

Comparing Fig. 15 to Figs. 12–14, the advantages of using SGA are very obvious. First of all, the final set of endmember pixels extracted by the SGA is always identical regardless of how many runs the SGA is conducted. Second of all, the endmember pixels extracted for a smaller value of p are always a subset of endmember pixels extracted for a larger value of p.

Finally, the impact of DR on the performance of EEAs was also investigated. Figs. 16–18 show that results of the PPI, N-FINDR, and SGA using three DR transforms for VD $= 9$ and SSE $= 10$. Unlike the synthetic image experiments in Section V where there was no difference among the three DR transforms to be used for preprocessing, the results in Figs. 16–18 provided evidence that it was important to choose an appropriate DR transform prior to endmember extraction. The experiments showed that using the ICA as a DR transform yielded the best performance where all the five distinct panel signatures were extracted as endmembers. Most importantly, the results also showed that VD $= 9$ was a better estimate than SSE $= 10$. As a matter of fact, according to Fig. 18, all the five panel signatures were extracted by the SGA using ICA before the eighth pixel was produced.

Like Table IV, Table VII also tabulates the computing time for PPI with 1000 skewers, N-FINDR, VCA, and SGA with

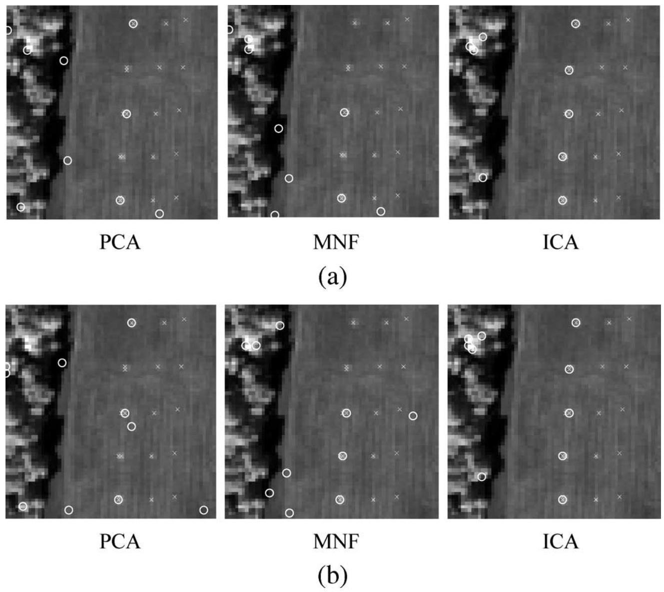

Fig. 17. Endmember pixels extracted by N-FINDR using three different DR transforms. (a) VD = 9. (b) SSE = 10.

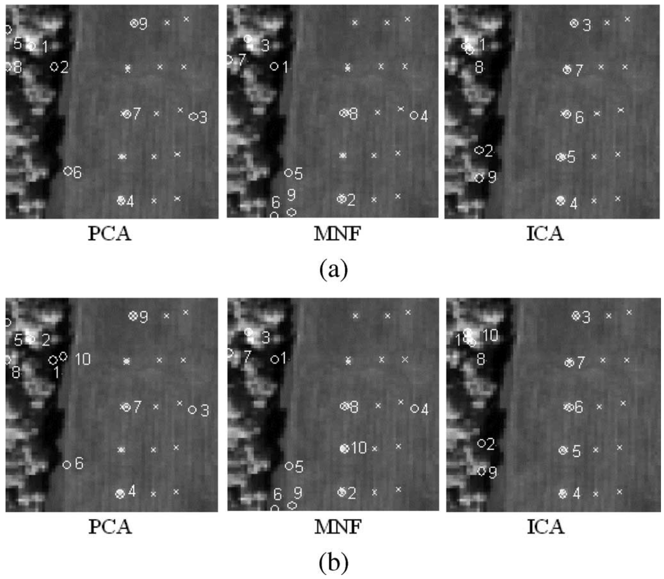

Fig. 18. Endmember pixels extracted by SGA using three different DR transforms. (a) VD = 9. (b) SSE = 10.

TABLE VII
COMPUTING TIME OF N-FINDR, VCA, AND SGA

Algorithm	PPI (1000 skewers)	N-FINDR	VCA	SGA
computing time	1.65 seconds	31.26 seconds	1.16 seconds	5.91 seconds

VD = 9 for the same computer environment in Table V where once again the PPI and VCA ran about five times faster than did the SGA and the SGA was five times faster than was N-FINDR. As indicated previously, this is because SGA calculated simplex volumes and required much more computing time than VCA did, which only calculated projections.

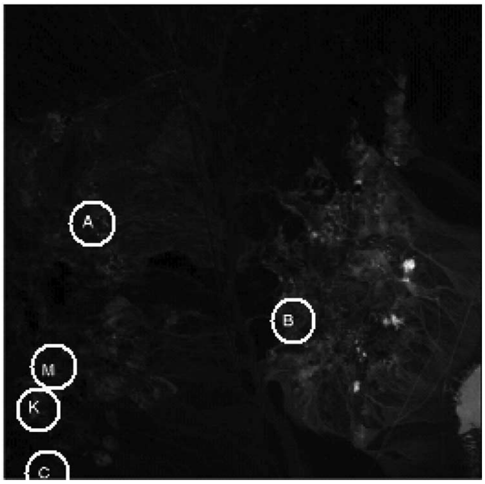

Fig. 19. Spatial positions of five pure pixels corresponding to minerals: alunite (A), buddingtonite (B), calcite (C), kaolinite (K), and muscovite (M).

TABLE VIII
VD ESTIMATES FOR THE CUPRITE SCENE IN FIG. 19 WITH VARIOUS FALSE ALARM PROBABILITIES

	$P_F = 10^{-1}$	$P_F = 10^{-2}$	$P_F = 10^{-3}$	$P_F = 10^{-4}$	$P_F = 10^{-5}$
VD	34	30	24	22	20

B. AVIRIS Cuprite Data

Another real image to be used for experiments is a well-known AVIRIS image scene, Cuprite, NV, shown in Fig. 19, which has been widely used to study endmember extraction extensively. It is available online [19] and was collected by 224 spectral bands with 10-nm spectral resolution over the Cuprite mining site, in 1997. The image has size of 350 × 350 pixels and is well understood mineralogically where bands 1–3, 105–115, and 150–170 have been removed prior to the analysis due to water absorption and low SNR in those bands. As a result, a total of 189 bands were used for experiments. The ground truth also provides the spatial locations of the five minerals, Alunite (A), Buddingtonite (B), Calcite (C), Kaolinite (K), and Muscovite (M) circled and labeled by A, B, C, K, and M, respectively, which can be used to verify endmembers extracted by an EEA.

The VD estimated for this image scene was tabulated in Table VIII with various false alarm probabilities.

For our experiments, VD was chosen to be 22. The selection of $p = 22$ is empirical based on the false alarm fixed at probabilities $P_F = 10^{-4}$. Also, the value of p estimated by the SSE was 28. The experiments were conducted based on these two values, i.e., $p = 22$ and 28 for comparative analysis.

Experiments similar to those conducted for HYDICE image scene in Section VI-A were also performed for the Cuprite image scene in Fig. 19.

First of all, Figs. 20–22 demonstrate a dilemma encountered in the PPI, N-FINDR, and VCA, which is that final results produced by these three algorithms in two different runs were inconsistent for both VD = 22 and SSE = 28. In these figures, the pixels marked by open circles were extracted by algorithms,

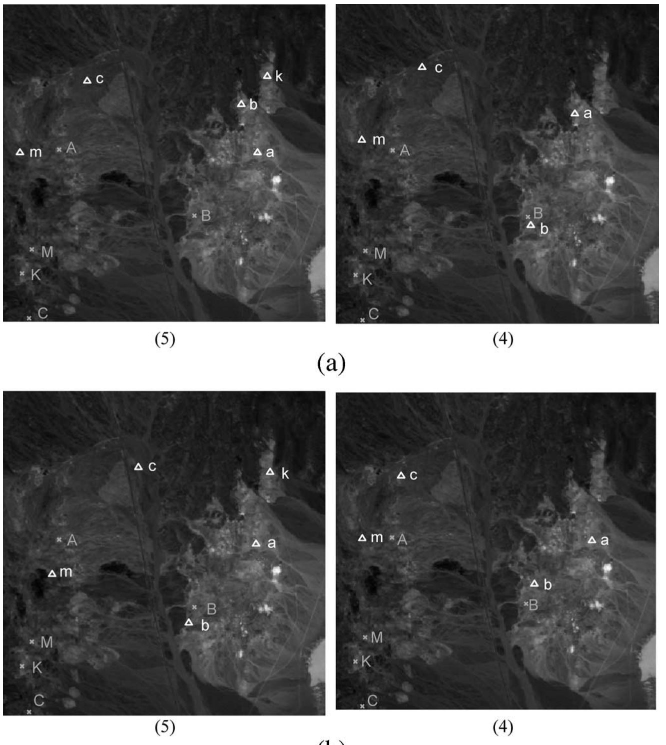

(5) (4)

(a)

(5) (4)

(b)

Fig. 20. Endmember pixels extracted by PPI in two different runs. (a) VD = 22. (b) SSE = 28.

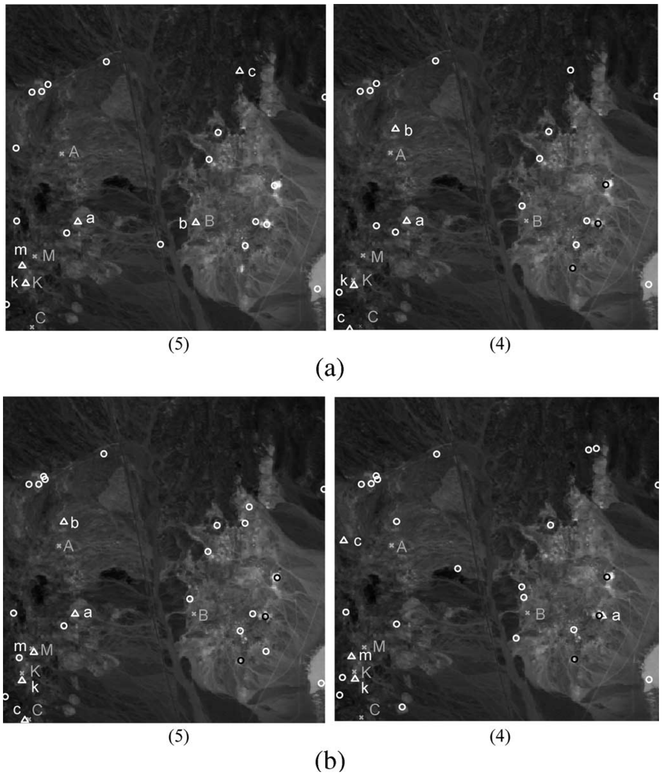

(5) (4)

(a)

(5) (4)

(b)

Fig. 21. Endmember pixels extracted by N-FINDR in two different runs. (a) VD = 22. (b) SSE = 28.

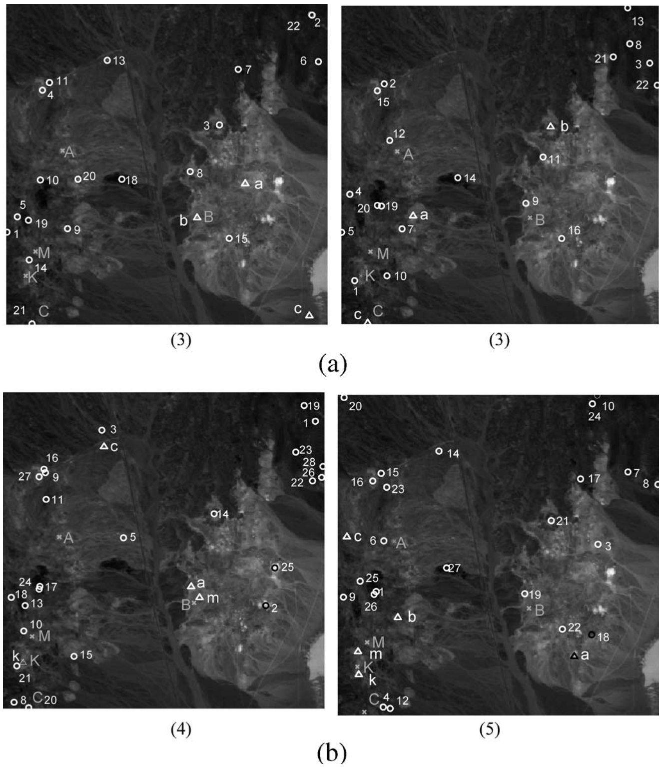

(3) (3)

(a)

(4) (5)

(b)

Fig. 22. Endmember pixels extracted by VCA in two different runs. (a) VD = 22. (b) SSE = 28.

and the pixels marked by the lower cases of “a, b, c, k, m” with triangles were the desired endmember pixels corresponding to the five ground truth mineral endmembers provided by [19] and marked by the upper cases of “A, B, C, K, M” with yellow crosses “x” in the sense of spectral similarity measured by the Spectral Angle Mapper (SAM) [1], [10]. Since similar tables using the SAM for signature matching can be obtained in the exact same manner that was performed in [17], the results are not included here to avoid replication. Therefore, in all the following experiments, only spatial locations of the extracted endmember pixels were identified and shown in the figures. Additionally, the numerals in open parentheses underneath these figures indicate the numbers of extracted endmember pixels that were identified in correspondence to ground truth mineral pixels by the SAM. Since the VCA is an SQEEA, the pixels in Fig. 22 labeled by numbers indicate the order that these pixels were extracted in sequence by VCA. It should be also noted that the PPI implemented here used 500 skewers for computational convenience.

As shown in Figs. 20 and 21, the PPI and the N-FINDR extracted different numbers of ground truth corresponding endmember pixels, 5 and 4 in two different runs for both cases, $\text{VD} = 22$ and $\text{SSE} = 28$. It was also true for the VCA with $\text{SSE} = 28$. Moreover, these extracted ground truth-corresponding endmember pixels were generally not the same. This is mainly due to the fact that there are other pixels whose spectral signatures are also similar and very close to ground truth mineral signatures. As a result, a different run is very much likely to extract different pixels corresponding to ground truth pixels. This evidence was demonstrated in Fig. 22(a) where the two sets of three endmember pixels corresponding to Alunite (A), Buddingtonite (B), Calcite (C) produced by

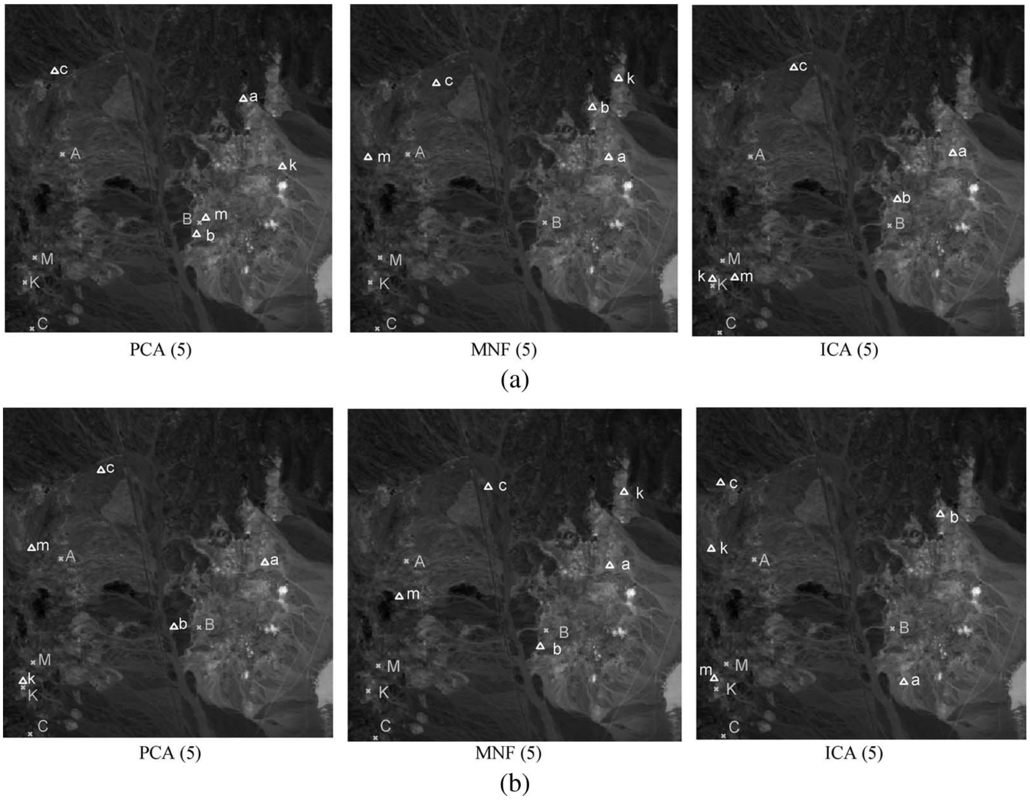

PCA (5) MNF (5) ICA (5)

(a)

PCA (5) MNF (5) ICA (5)

(b)

Fig. 23. Endmember pixels extracted by PPI using three DR transforms using 500 skewers. (a) VD = 22. (b) SSE = 28.

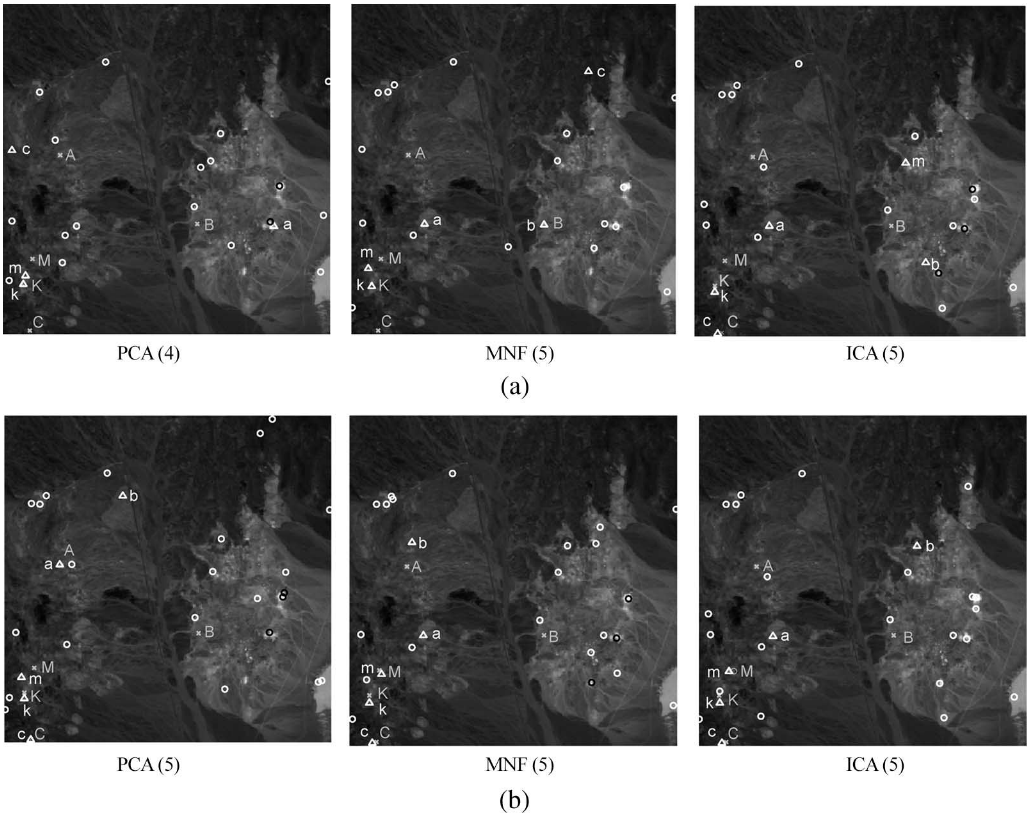

PCA (4) MNF (5) ICA (5)

(a)

PCA (5) MNF (5) ICA (5)

(b)

Fig. 24. Endmember pixels extracted by N-FINDR using three DR transforms. (a) VD = 22. (b) SSE = 28.

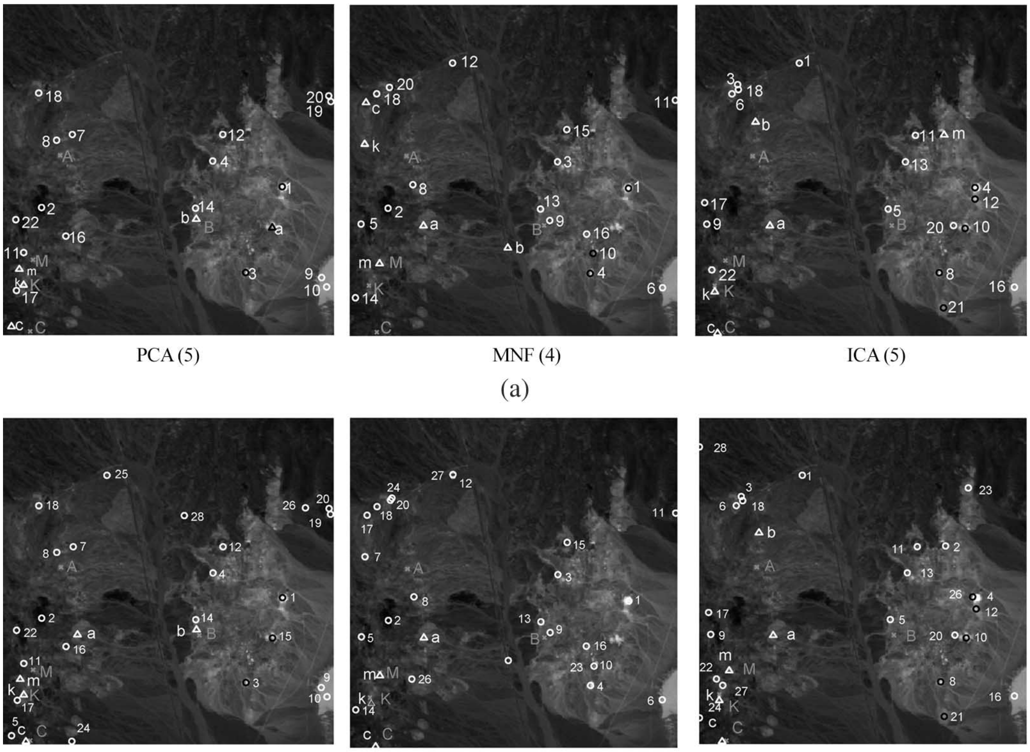
PCA (5) MNF (4) ICA (5)

(a)

PCA (5) MNF (4) ICA (5)

(b)

Fig. 25. Endmember pixels extracted by SGA using three DR transforms. (a) VD = 22. (b) SSE = 28.

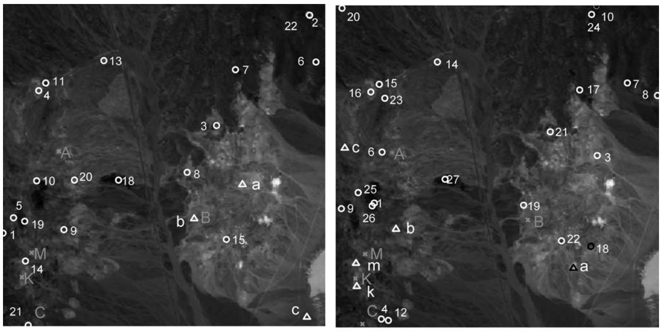
(3) (5)

(a) (b)

Fig. 26. Endmember pixels extracted by VCA. (a) VD = 22. (b) SSE = 28.

the VCA in Fig. 22(a) for VD = 22 in two separate runs were different.

So far, we have demonstrated a major drawback of the use of randomly generated initial endmembers. Next, we conducted a comparative analysis and performance evaluation among the four EEAs, two SMEEAs (PPI and N-FINDR) and two SQEEAs (VCA and SGA). Since all the four studied EEAs required DR as a preprocessing, three DR transforms used in previous experiments were also used for the following experiments. Figs. 23–25 show the results of endmembers extracted by PPI with 500 skewers, N-FINDR, SGA using three DR transforms, PCA, MNF, and ICA for VD = 22 and SSE = 28, respectively, where notations used in these figures are the same as those used in Figs. 20–22.

As noted earlier, since the VCA has its built-in DR transform, no experiments on these three DR transforms conducted for VCA. Fig. 26 also showed the results obtained by the VCA for VD = 22 and SSE = 28.

By examining results in Figs. 23–26, the PPI, N-FINDR, SGA, and VCA could extract all desired five pixels that corresponded to ground truth pixels in terms of spectral similarity measured by the SAM for both VD = 22 and SSE = 28. On some occasions, there were four endmembers extracted such as Fig. 24(a) with the PCA and Fig. 25(a) and (b) with the MNF. However, these could be corrected by ICA, which consistently yielded the best results in all cases. Interestingly, Fig. 25(a) and (b) also showed that when the SGA was implemented with the MNF, only four ground truth corresponding pixels were extracted even SSE used a higher value of $p = 28$ than 22 estimated by the VD. This implied that according to our experiments, the SSE seemed to overestimate the number of endmembers, 28 which was higher than 22 estimated by VD. Most importantly, all experiments conducted above demonstrated that our proposed SGA performed at least comparably with other EEAs with one major advantage, which other EEAs do not have, consistent final set of selected endmembers.

Finally, Table IX also tabulates the computing time for PPI with 500 skewers, N-FINDR, VCA, and SGA with VD = 22 for the same computer environment in Table V. As we can see, the projection-based algorithms PPI and VCA showed significant savings in computing time compared to simplex volume-based algorithms SGA and N-FINDR. Nevertheless, the SGA was five times faster than the N-FINDR.

TABLE IX
COMPUTING TIME OF N-FINDR, VCA, AND SGA

Algorithm	PPI (500 skewers)	N-FINDR	VCA	SGA
computing time	11.52 seconds	3456.1 seconds	10.77 seconds	594.5 seconds

VII. CONCLUSION

This paper introduces a new simplex growing method, an SGA that resolves three major issues encountered in the N-FINDR: 1) determination of the number of endmembers; 2) inconsistent final selection set of endmembers; and 3) computational complexity. Coincidentally, the idea of growing simplexes to find endmembers used in the SGA is similar to that used in a recently developed VCA, but their approaches are different. Most distinctly, the VCA still cannot address the second issue, which is inconsistent results in finding a desired set of endmembers due to its use of random projections for simplexes generated by zero-mean Gaussian distributions as a simplex grows.

As a final concluding remark, there is a commercial version of the N-FINDR that is available [20] which also resolves the second and the third issues. Unfortunately, the details of its implementation are not made available to users. In particular, it does not allow users to select their own initial endmembers for comparison. Therefore, it was not studied in this paper. Nevertheless, computational complexity given in Table I remains the same. Additionally, since it is believed to be written in C not MATLAB, the computation is expected to be much faster than the one using MATLAB in this paper. It is our belief that if our proposed SGA is also written in C, its computation can be significantly improved and comparable to the commercial version of the N-FINDR.

ACKNOWLEDGMENT

The authors would like to thank Dr. Nascimento who provided his developed VCA to be implemented in this paper. The authors would also like to thank the anonymous reviewers who suggested the use of a different DR transform for comparative analysis and to provide the reference [14].

REFERENCES

[1] R. A. Schowengerdt, *Remote Sensing: Models and Methods for Image Processing*, 2nd ed. New York: Academic, 1997.

[2] J. W. Boardman, F. A. Kruse, and R. O. Green, "Mapping target signatures via partial unmixing of AVIRIS data," in *Proc. Summ. JPL Airborne Earth Sci. Workshop*, Pasadena, CA, 1995, pp. 23–26.

[3] M. E. Winter, "N-finder: An algorithm for fast autonomous spectral endmember determination in hyperspectral data," in *Proc. Image Spectrom. V*, 1999, vol. 3753, pp. 266–277.

[4] R. A. Neville, K. Staenz, T. Szeredi, J. Lefebvre, and P. Hauff, "Automatic endmember extraction from hyperspectral data for mineral exploration," in *Proc. 4th Int. Airborne Remote Sens. Conf. and Exhib./21st Can. Symp. Remote Sens.*, Ottawa, ON, Canada, Jun. 1999, pp. 21–24.

[5] A. Plaza, P. Martinez, R. Perez, and J. Plaza, "Spatial/spectral endmember extraction by multidimensional morphological operations," *IEEE Trans. Geosci. Remote Sens.*, vol. 40, no. 9, pp. 2025–2041, Sep. 2002.

[6] M. D. Craig, "Minimum-volume transforms for remotely sensed data," *IEEE Trans. Geosci. Remote Sens.*, vol. 32, no. 3, pp. 542–552, May 1994.

[7] J. W. Boardman, "Geometric mixture analysis of imaging spectrometery data," in *Proc. Int. Geosci. Remote Sens. Symp.*, 1994, vol. 4, pp. 2369–2371.

[8] A. Ifarraguerri and C.-I Chang, "Hyperspectral image segmentation with convex cones," *IEEE Trans. Geosci. Remote Sens.*, vol. 37, no. 2, pp. 756–770, Mar. 1999.

[9] J. M. P. Nascimento and J. M. Dias, "Vertex component analysis: A fast algorithm to unmix hyperspectral data," *IEEE Trans. Geosci. Remote Sens.*, vol. 43, no. 4, pp. 898–910, Apr. 2005.

[10] C.-I Chang, *Hyperspectral Imaging: Techniques for Spectral Detection and Classification*. Norwell, MA: Kluwer, 2003.

[11] C.-I Chang and Q. Du, "Estimation of number of spectrally distinct signal sources in hyperspectral imagery," *IEEE Trans. Geosci. Remote Sens.*, vol. 42, no. 3, pp. 608–619, Mar. 2004.

[12] J. Wang and C.-I Chang, "Dimensionality reduction by independent component analysis for hyperspectral image analysis," in *Proc. IEEE Int. Geosci. Remote Sens. Symp.*, Seoul, Korea, Jul. 25–29, 2005.

[13] C.-I Chang and A. Plaza, "Fast iterative algorithm for implementation of pixel purity index," *IEEE Geosci. Remote Sens. Lett.*, vol. 3, no. 1, pp. 63–67, Jan. 2006.

[14] J. Dias and J. Nascimento, "Estimation of signal subspace on hyperspectral data," in *Proc. SPIE*, Sep. 2005, vol. 5982, pp. 191–198.

[15] J. C. Harsanyi and C.-I Chang, "Hyperspectral image classification and dimensionality reduction: An orthogonal subspace projection approach," *IEEE Trans. Geosci. Remote Sens.*, vol. 32, no. 4, pp. 779–785, Jul. 1994.

[16] F. Chaudhry, C. Wu, W. Liu, C.-I Chang, and A. Plaza, "Pixel purity index-based algorithms for endemember extraction from hyperspectral imagery," in *Recent Advances in Hyperspectral Signal and Image Processing*, C.-I Chang, Ed. Trivandrum, India: Research Signpost, 2006, ch. 3.

[17] J. Wang and C.-I Chang, "Independent component analysis-based dimensionality reduction with applications in hyperspectral image analysis," *IEEE Trans. Geosci. Remote Sens.*, vol. 44, no. 6, pp. 1586–1600, Jun. 2006.

[18] R. E. Roger and J. F. Arnold, "Reliably estimating the noise in AVIRIS hyperspectral imagers," *Int. J. Remote Sens.*, vol. 17, no. 10, pp. 1951–1962, 1996.

[19] [Online]. Available: http://speclab.cr.usgs.gov/cuprite.html and http://aviris.jpl.nasa.gov/html/aviris.free.data.html

[20] A. J. Plaza, P. Martinez, A. Plaza and R. M. Perez "Quantifying the impact of spatial resolution on endmember extraction from hyperspectral imagery," in *Proc. 3rd EARSeL Workshop Imag. Spectrosc.*, Germany, 2003, pp. 117–125.

Chein-I Chang (S'81–M'82–SM'92) received the B.S. degree in mathematics from Soochow University, Taipei, Taiwan, R.O.C., in 1973, the M.S. degree in mathematics from the Institute of Mathematics, National Tsing Hua University, Hsinchu, Taiwan, R.O.C., in 1975, the M.A. degree in mathematics from the State University of New York, StonyBrook, in 1977, the M. S. and M.S.E.E. degrees from the University of Illinois, Urbana-Champaign, in 1982, and the Ph.D. degree in electrical engineering from the University of Maryland, College Park, in 1987.

Since 1987, he has been with UMBC as a Visiting Assistant Professor from January 1987 to August 1987, Assistant Professor from 1987 to 1993, Associate Professor from 1993 to 2001, and Professor in the Department of Computer Science and Electrical Engineering since 2001. From 1994 to 1995, he was a Visiting Research Specialist in the Institute of Information Engineering at the National Cheng Kung University, Tainan, Taiwan. He was a Distinguished Lecturer at the National Chung Hsing University, Taichung, Taiwan, sponsored by the Ministry of Education, from 2005 to 2006. He was on the Editorial Board of the *Journal of High-Speed Networks* and was the Guest Editor of a special issue of the same journal on telemedicine and applications. He is the author of *Hyperspectral Imaging: Techniques for Spectral Detection and Classification* (New York: Kluwer, 2003). He has three patents and several pending patents. His research interests include multispectral/hyperspectral image processing, automatic target recognition, medical imaging, information theory and coding, signal detection and estimation, and neural networks.

Dr. Chang received a National Research Council Senior Research Associateship Award from 2002 to 2003, sponsored by the U.S. Army Soldier and Biological Chemical Command, Edgewood Chemical and Biological Center. He is an Associate Editor in the area of hyperspectral signal processing for the IEEE TRANSACTIONS ON GEOSCIENCE AND REMOTE SENSING. He is a Fellow of the International Society for Optical Engineering and a member of Phi Kappa Phi and Eta Kappa Nu.

Chao-Cheng Wu (S'04) received the B.S. degree in electrical engineering from Tamkang University, Taipei, Taiwan, R.O.C., in 2002 and the M.S. degree in electrical engineering from the University of Maryland, Baltimore County (UMBC), Baltimore, in 2006.

He is currently a Research Assistant in the Remote Sensing, Signal, and Image Processing Laboratory at UMBC. His research interests include signal and hyperspectral image processing.

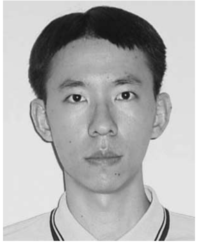

Wei-min Liu (S'03) received the B.S. degree in applied mathematics from the National Chiao Tung University, Taiwan, R.O.C., in 2001, and the M.S. degree in electrical engineering from the University of Maryland, Baltimore County (UMBC), Baltimore, in 2005. He is currently working toward the Ph.D. degree at UMBC.

He is currently a Research Assistant in the Remote Sensing, Signal, and Image Processing Laboratory, UMBC. His research interests include multi/hyperspectral and medical image processing, pattern recognition, and adaptive signal processing.

Yen-Chieh Ouyang (S'86–M'92) received the B.S.E.E. degree from Feng Chia University, Taichung, Taiwan, in 1981, and the M.S. and Ph.D. degrees, both from University of Memphis, Memphis, Tennessee, in 1987, and 1992, respectively, all in electrical engineering.

He joined the faculty of the Department of Electrical Engineering at National Chung Hsing University (NCHU), Taichung, Taiwan, R.O.C., in August 1992. He is currently an Associate Professor and the Director of the Multimedia Communication Laboratory, NCHU. His research interests include hyperspectral image processing, communication networks, providing QoS over wireless and network security in mobile networks, multimedia system design, and performance evaluation.